Journal of Power Sources 192 (2009) 344–352

Contents lists available at ScienceDirect

Journal of Power Sources

journal homepage: www.elsevier.com/locate/jpowsour

Solid Oxide Fuel Cells damage mechanisms due to Ni-YSZ re-oxidation: Case of the Anode Supported Cell

J. Laurencin[a,*], G. Delette[a], B. Morel[a], F. Lefebvre-Joud[a], M. Dupeux[b]

[a] CEA/LITEN/DTH/LEV, 17 avenue des martyrs 38054 Grenoble, France
[b] SIMAP (INP Grenoble/CNRS/UJF), BP 75 38402 Saint Martin d'Hères, France

ARTICLE INFO

Article history:
Received 22 December 2008
Received in revised form 29 January 2009
Accepted 27 February 2009
Available online 14 March 2009

Keywords:
SOFC
Cermet Ni-YSZ
Re-oxidation
Degradation
Impedance spectroscopy

ABSTRACT

The effects of Ni-YSZ cermet re-oxidation in anode supported Solid Oxide Fuel Cells (SOFCs) have been investigated. Damage mechanisms have been studied in both cases of direct oxidation in air (*i.e.*, fuel shutdown) or by an ionic current (*i.e.*, fuel starvation).

Direct oxidation tests show that the electrolyte cracks for a conversion degree of Ni into NiO ranging between ~58 and ~71%. This failure mode has been modelled considering both the bulk expansion of the cermet induced by the transformation of the Ni phase and the change of mechanical stresses in the multilayered cell.

In the case of fuel starvation, a thin layer of the cermet was electrochemically re-oxidised at 800 °C and then reduced under a hydrogen stream. This 'redox' cycle was repeated until the degradation of the cell. The evolution of the impedance diagrams recorded after each cycle suggests that the cermet damages in an area close to anode/electrolyte interface. The mechanical modelling states that a delamination can occur along the interface between the Anode Functional Layer (AFL) and the Anode Current Collector (ACC) substrate. This theoretical result confirms the experimental trends observed by impedance spectroscopy.

1. Introduction

Solid Oxide Fuel Cells (SOFCs) allow the conversion of fuel chemical energy into electricity. These devices operate at high temperatures and represent an attractive and efficient technology for power generation. The configuration of Anode Supported Cell (ASC) presents high electrochemical performances and is especially interesting for an operation including Direct Internal Reforming (DIR) of methane.

Nowadays, the main issue before the SOFCs commercialisation consists in improving the reliability and durability of this technology.

More particularly, it has been pointed out that the performances of ASC design are sharply reduced when the usual anode material (Ni/YSZ cermet) operates under alternatively oxidising and reducing conditions at elevated temperature ('redox' cycles).

Such cycles may occur as a result of repeated start and shutdown operations. Indeed, when the fuel supply is interrupted at high temperature, air may enter the anode compartment and partially oxidise the cermet.

ASC designed with a thick substrate of Ni/YSZ cermet supporting the thin electrolyte (YSZ) and cathode layers has been widely studied. Many authors reported some important electrochemical degradation after only one or few 'redox' cycles [1–4].

This degradation has been related to mechanical damage of the cell induced by the oxidation of Ni into NiO. Indeed, this transformation is accompanied by a macroscopic cermet bulk expansion [5–7] depending mainly on its degree of oxidation [8] or microstructure parameters such as porosity or Ni content [6]. The anodic strain can induce high tensile stresses in the thin electrolyte and cathode layers. This loading leads to an electrolyte mechanical failure [9] even for partial anode re-oxidation. Models have been recently developed to understand and predict these mechanical degradations. In a previous study, the authors used a numerical modelling [10] to describe the ASC failure modes. It has been shown that the cathode fracture seems to be unavoidable, whereas electrolyte cracking is expected when the anodic strain reaches ~0.15%. This result has been found to be in good agreement with the analytical approach performed by Sarantaridis and Atkinson [11,12].

Another operating condition can be involved in the cermet re-oxidation: it occurs when the fuel supply is not sufficient regarding to the requested electrical power. In this case, the O^{2-} oxide ions passing through the electrolyte oxidise a thin cermet layer growing from the anode/electrolyte interface. Few studies have been dedicated to this mechanism [13,14]. For instance, Hatae et al. [14]

* Corresponding author. Tel.: +33 4 38782210; fax: +33 4 38784139.
E-mail address: laurencin@chartreuse.cea.fr (J. Laurencin).

0378-7753/$ – see front matter © 2009 Elsevier B.V. All rights reserved.
doi:10.1016/j.jpowsour.2009.02.089

have shown that the Ni particles re-oxidation under ionic current leads to an electrolyte stress relaxation. However, electrochemical degradations and mechanical damages are not well established yet.

The present article deals with both mechanisms inducing anode re-oxidation. Its main objective is to propose a methodology to state the SOFC degradations due to the cermet oxidation. This methodology has been used to assess cells behaviour provided by the Forschungszentrum Jülich (FZJ) research centre.

- Case of cermet oxidation due to an air stream: this section aims at determining the critical anodic strain which induces electrolyte rupture. The value has been measured and compared to the model prediction. The experimental part consisted in performing gradual re-oxidation of ASC. At each step of the re-oxidation, the cell integrity has been controlled in order to detect the cracking threshold.
- Case of cermet oxidation under ionic current: the purpose of this section is to highlight the electrochemical degradation of the cell and to establish the relation with the mechanical damage. A thin layer of the anode substrate has been electrochemically oxidised and then reduced. This 'redox' cycle has been repeated, and the decay of cell performance has been continuously recorded by impedance spectroscopy. The degradation has been discussed on the basis of a numerical mechanical modelling.

2. Experimental

2.1. Samples description

Experiments have been conducted using Anode Supported Cells supplied by FZJ research centre. All the tested samples are circular in shape with a diameter of 55 mm. The anode includes a thin Anode Functional Layer (AFL) deposited on an Anode Current Collector (ACC) which is the substrate supporting the cell. It is approximately 1.5 mm thick and constituted of 56 wt.% NiO and 44 wt% 8YSZ (ZrO_2 stabilised with 8% mol Y_2O_3). The ACC cermet porosity is equal to around ~23% in the fully oxidised state (and ~43% in the reduced state).

The AFL and the dense electrolyte (8YSZ) are co-sintered together with the support and both have a thickness of ~10 μm. AFL is almost fully dense when Ni particles are oxidised. Cathode has a diameter of 40 mm and is centred on the electrolyte. This layer has a thickness of about ~50 μm. It is constituted by a Cathode Functional Layer (CFL) on which is applied a current collector of pure LSM (Lanthanum doped Strontium Manganite). The CFL presents a thickness of ~15 μm and is composed of 50 wt.% LSM and 50 wt.% 8YSZ.

2.2. Test procedures

2.2.1. Anode re-oxidation by an air stream (fuel shutdown)

In order to simulate anode re-oxidation by an air stream, free standing single cells were placed into the chamber of a furnace which can be swept by various gaseous species. Anode partial re-oxidations were conducted at 800 °C according to the procedure depicted in Fig. 1. Cells were heated up to 800 °C at a rate of 5 °C min^{-1} under 2%H_2 + Ar. In order to achieve the initial complete cermet reduction, the cells were maintained on temperature under this gas feeding during 36 h. This procedure has been qualified by RX diffraction spectra indicating that all the Ni species are present under metallic form.

Following the initial reduction step, gas supply was switched to air at 800 °C and maintained during a fixed time. The cooling down to the room temperature was performed at a rate of 5 °C min^{-1}. This step is performed under Ar sweeping to avoid any change in the

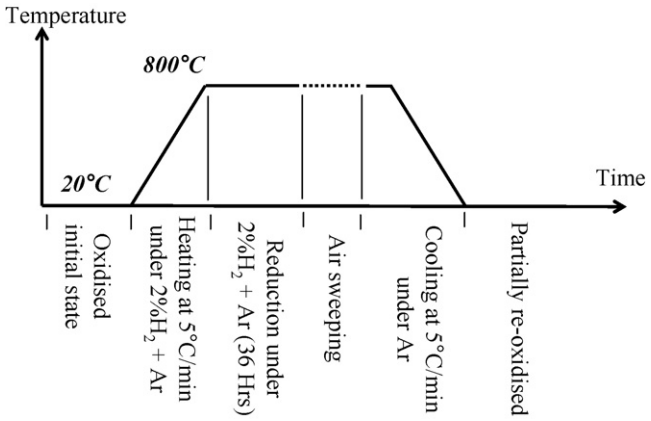

Fig. 1. Sequences used to partially re-oxidise the cermet by air sweeping.

Nickel state oxidation. The degree of oxidation was finally estimated by measuring the increase in weight of the sample.

The relation between the degree of oxidation and the anodic linear strain was determined by using the experimental curve established by Sarantaridis et al. [13] on FZJ–ASC cells (Fig. 2). The reliability of this curve for the cermet used in the present study has been verified. For this purpose, two marks have been done on the anode surface by Vickers indentation. The linear strain was estimated by measuring the spacing before and after the cermet oxidation. A good agreement has been obtained between this measurement and the curve established by Sarantaridis et al. [13].

For each degree of oxidation, the mechanical integrity of the electrolyte layer has been assessed by testing its gas tightness. The He-permeability of the cell has been measured at room temperature by using the test bench depicted in Fig. 3. The cell is placed between two polymeric joints in a stainless steel sample holder. The upper flange is screwed on the inferior one to clamp the cell and the two joints. A Helium flow rate is imposed at the cathode side whereas a Nitrogen flux sweeps the anode compartment. A mass spectrometer is plugged at the anode side and allows measuring the He molar flow rate crossing through the electrolyte layer.

2.2.2. Anode re-oxidation by an ionic current (fuel starvation)

Electrochemical experiments have been performed in the test bench described in Fig. 4. Ceramic glass is used to seal the cell in a holding ring made of alumina. The cell and its ceramic support are introduced into the test bench housing in which two gold seals ensure the complete tightness of the cathodic and anodic

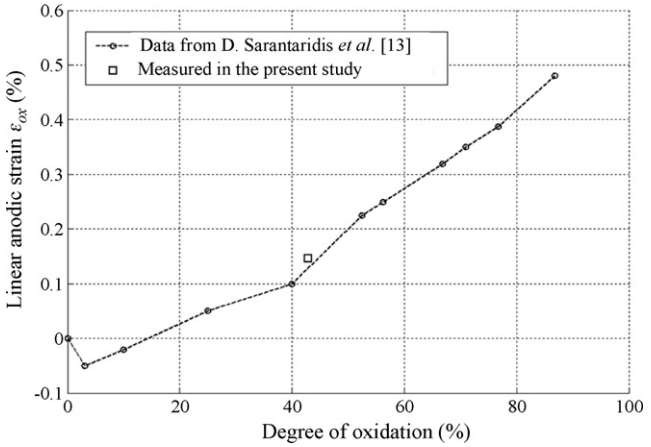

Fig. 2. Linear strain of the cermet substrate plotted as function of its degree of oxidation.

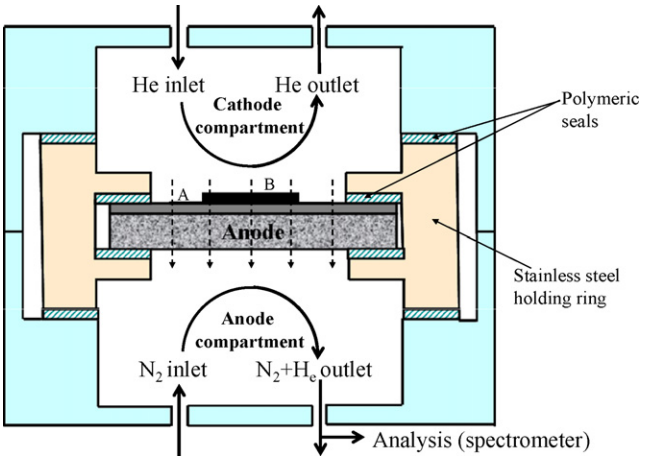

Fig. 3. Scheme of the test rig employed to measure the electrolyte permeability. *Area A:* the electrolyte is not covered by the cathode. *Area B:* the cathode covers the electrolyte.

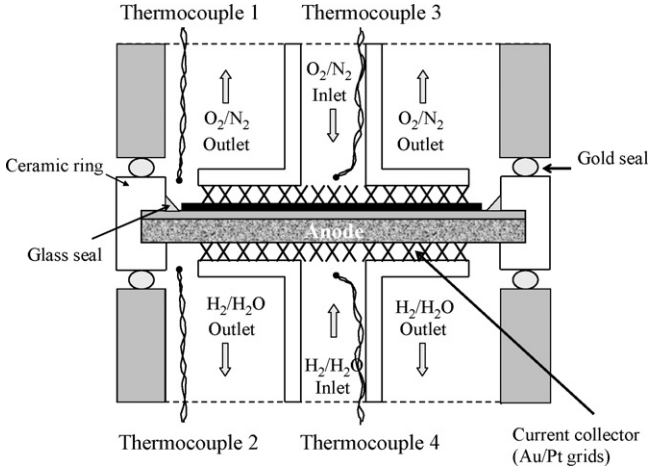

Fig. 4. Schematic representation of the electrochemical test bench.

compartments. This mounting prevents any leakage of oxygen into the anodic channel and thus ensures that the re-oxidation of the cermet is only due to electrochemical reactions. It is worth to underline that the glass seal is viscous at the operating temperature (800 °C), and, hence, the cell can be considered free of external loading. Therefore, the sample does not suffer from severe stress due to the fixing into the ceramic holder during the test.

Air and fuel channels present a radial co-flow arrangement where fluids are introduced at the cell centre and are exhausted from its periphery. A coarse gold mesh covered by a fine Pt mesh (3600 square cm^{-2}) is laid on each electrode to collect the current. A load (~200 g cm^{-2}) is applied on the grids in order to improve the electron collection.

After the initial reduction of the NiO phase, the cermet was electrochemically oxidised by stopping the H_2 supply and by imposing an ionic current through the cell for a given time. The flux of oxygen ions passing through the electrolyte and reaching the anode induces the oxidation of the Ni phase according to the following reaction:

$$Ni + O^{2-} \rightarrow NiO + 2e^{-} \quad (1)$$

The growth of the oxidised layer (NiO-YSZ) is initiated at the anode/electrolyte interface .

After this oxidation step, the cermet was reduced once again under hydrogen. This 'redox' cycle has been repeated nine times at 800 °C. Each cycle has been carried out considering the following sequences:

(i) *Operation under reducing conditions*: humidified hydrogen (H_2 + 3%H_2O) is send to the anode side at a flow rate of N_{H_2} = 17.5 ml min^{-1} cm^{-2},
(ii) *Decrease in the fuel supply*: the anodic compartment is swept under (Ar + 10%H_2) for 10 min (N_{Ar} = 3.6 ml min^{-1} cm^{-2}),
(iii) *Operation under oxidising conditions*: the fuel supply is stopped while a current density of 80 mA cm^{-2} is imposed during a given time Δt. The duration Δt of the oxidation dwell is given in Table 1.

The cell electrochemical response has been followed by monitoring the cell voltage during the test. The evolution of the cell resistance has been estimated by impedance spectroscopy. Diagrams have been recorded under hydrogen (*i.e.*, between two oxidising steps) at the Open Circuit Voltage (OCV). Impedance data have been obtained within the range of frequency (10 kHz–0.01 Hz) with an applied current density of Δi = 9.6 mA cm^{-2}.

3. Results and data analysis

3.1. Anode re-oxidation induced by an air stream (fuel shutdown)

Helium fluxes crossing the partially re-oxidised cells have been measured during permeability tests. It can be observed in Fig. 5 that the flux is not significant when the cermet degree of oxidation is equal to ~38% or ~58%. In these cases, the residual leakage corresponds to the value measured on intact cells before the test. This

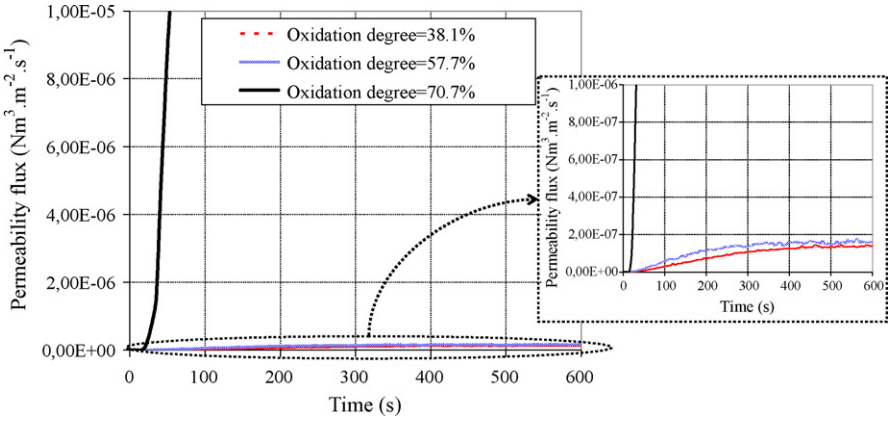

Fig. 5. Helium permeability flux crossing the electrolyte plotted as a function of time. The curves are related to three oxidation degree of the cermet.

Table 1
Duration of each oxidising dwell and h/h_{anode} ratio (with h_{anode} = 1.5 mm).

	Cycle number								
	1	2	3	4	5	6	7	8	9
Duration of the oxidising step Δt (min)	20	20	20	27	37	58	30	36	33
h/h_{anode} ratio	0.08	0.08	0.08	0.11	0.15	0.23	0.12	0.14	0.13

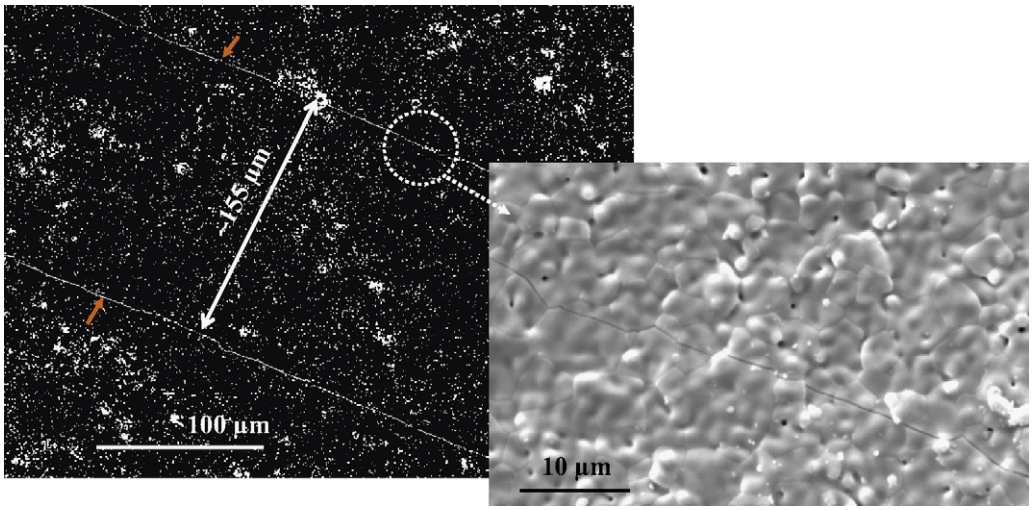

Fig. 6. SEM observation of the electrolyte surface (Area A of the cell: cf. Fig. 3) for ~71% degree of oxidation. In order to improve the visualisation of cracks, the image has been processed by a grey-level thresholding.

result means that the electrolyte has not been damaged as it has remained nearly gas tight.

On the contrary, for an oxidation degree of ~71%, the electrolyte layer became permeable to gas, since the permeability flux is found to be very high and exceeds the measuring range of the mass spectrometer. It can be reasonably inferred that the electrolyte layer was cracked. This result is confirmed by surface observations of the electrolytic layer with a Scanning Electron Microscope (SEM): observations have revealed a pattern of parallel cracks typical of a channel cracking mode (Fig. 6). The parallel direction of these cracks (instead of a random-oriented crack pattern as expected under an equi-biaxial stress state) may be due to some anisotropy in the toughness properties of the electrolyte layer, consecutive to its manufacturing process by vacuum slip casting [15].

The electrolyte damage has occurred for oxidation degree ranging between ~58 and ~71%. Considering the curve provided in Fig. 2, it can be deduced that the electrolyte fracture has arisen for oxidation strain higher than 0.26% and lower than 0.34%.

3.2. Anode re-oxidation induced by an ionic current (fuel starvation)

3.2.1. Initial cell performances

The cell polarisation curve has been measured under wet (3%H_2O) hydrogen at T = 800 °C. It can be noticed in Fig. 7 that reasonable electrochemical performances are achieved. Indeed, the current density reaches 730 mA cm^{-2} for a cell voltage equal to 0.7 V and a fuel utilisation of 31.5%.

3.2.2. Cell voltage measurement during the 'redox' cycles

Fig. 8 exhibits the typical evolution of the cell voltage recorded during one 'redox' cycle. It can be observed that the voltage falls down as soon as the fuel supply is simultaneously stopped and the ionic current is imposed through the electrolyte. In a first time, the remaining hydrogen stored in the anodic channel is consumed. When the cell voltage reaches ~0.7 V, a discontinuity in the slope of the curve is observed. Indeed, this value corresponds to the theoretical OCV for the NiO, Ni//Air system at 800 °C:

$$OCV^{Ni+1/2O_2 \leftrightarrow NiO} = \frac{RT}{4F} \ln \frac{P_{O_2}^{air}}{P_{O_2}^{fuel}} \quad (2)$$

where T denotes the temperature, R the gas constant and $P_{O_2}^{fuel}$ the oxygen partial pressure in air ($P_{O_2}^{fuel} = 0.21$). The term $P_{O_2}^{fuel}$ is equal to the oxygen partial pressure in the anodic compartment determined at the Ni(s)+1/2O_2 ↔ NiO(s) chemical equilibrium:

$$P_{O_2}^{eq} = \exp\left(\frac{2\Delta G_{Ni/NiO}^{0}(T)}{RT}\right) \quad (3)$$

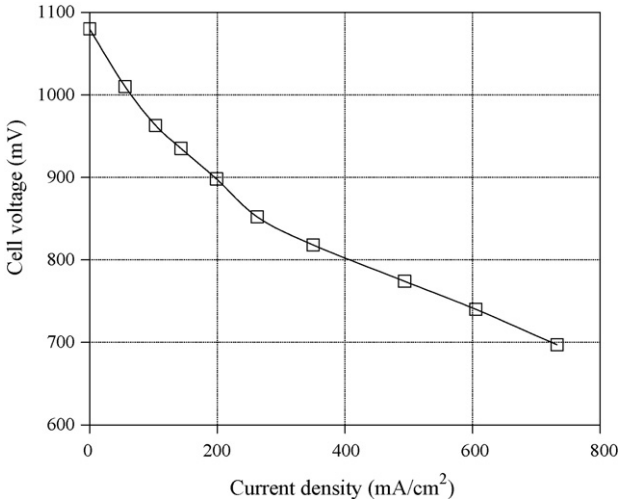

Fig. 7. Polarisation curves measured at T = 800 °C under wet hydrogen (N_{H_2} = 17.5 ml min^{-1} cm^{-2}, N_{H_2O} = 0.54 ml min^{-1} cm^{-2}, N_{Air} = 42.4 ml min^{-1} cm^{-2}).

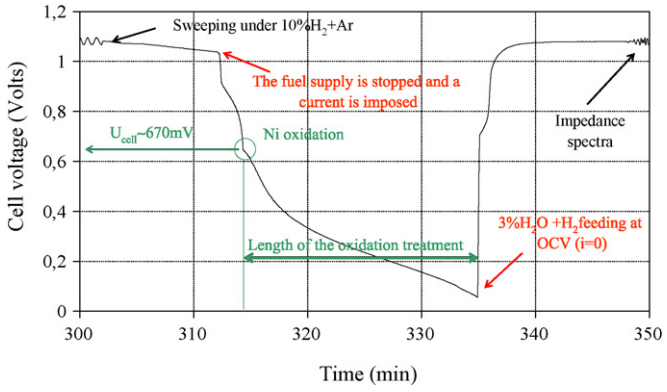

Fig. 8. Typical evolution of the cell voltage during one 'redox' cycle (T = 800 °C, cycle no. 1).

where $\Delta G^0_{Ni/NiO}$ is the standard Gibbs energy of formation of NiO (=−143095 J mol^{-1} at 800 °C [16]). Below the threshold of 0.7 V, Ni is used as fuel and transformed into NiO. Although the current density is imposed to a constant level, the cell voltage is found to decrease continuously during the oxidising step without reaching a dwell. This evolution is explained by the growth of the NiO electrical insulating layer. Indeed, the thickening of the oxidised layer leads to an increase in the anodic ohmic resistance of the cell.

The measured OCV is assessed to ~1.08 V under reducing operation (Fig. 8) and corresponds to the theoretical value for H_2O, H_2/Air system at 800 °C. This OCV level has been kept constant under hydrogen after all the oxidising treatments carried out during the test. This last result means that electrolyte layer is remained gas tight to prevent the direct combustion of hydrogen in air, and suggests that the electrolyte has not been cracked during the test.

3.2.3. *Impedance spectroscopy measurements*

A typical diagram obtained by impedance spectroscopy under normal conditions (3%H_2O + H_2) is plotted in Fig. 9 according the Nyquist representation. The imaginary part Z'' of the cell impedance is plotted as a function of the real part Z′ for all investigated frequencies.

At the highest frequencies, the diagram is constituted by an inductance in serial with a resistance (noted R_{HF}). Inductance is

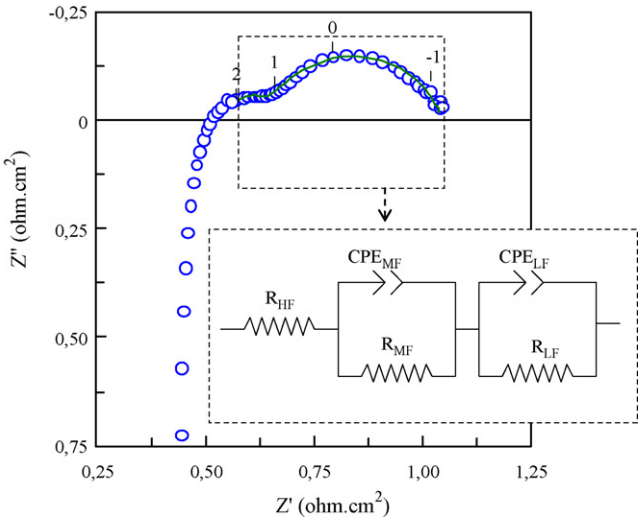

Fig. 9. Typical impedance diagram obtained under wet hydrogen at 800 °C (cycle no. 1). The diagram has been plotted in the complex plane. The numbers mark the decimal logarithm of the frequency. The equivalent circuit used for the fit is represented: the fit result corresponds to the solid line.

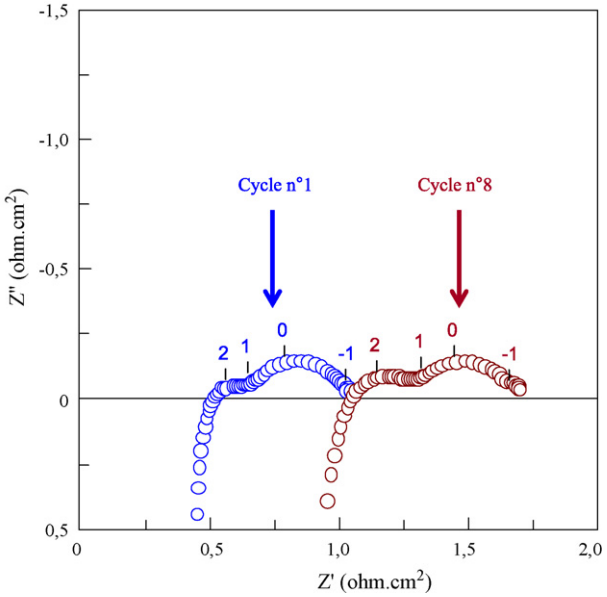

Fig. 10. Comparison between the impedance diagrams recorded after the first 'redox' cycle and the eighth 'redox' cycle. The diagrams have been plotted in the complex plane. The numbers mark the decimal logarithm of the frequency.

caused by the interactions between the electrical wires of the test bench. The ohmic contribution R_{HF} is classically attributed to the sum of two resistances: the current collecting resistance and the ionic resistance of the electrolyte.

The high frequency cell response is followed on the diagram by two semicircles at medium and low frequencies. Both semicircles are induced by the electrochemical processes occurring at the electrodes.

An equivalent circuit presented in Fig. 9 is proposed to fit the impedance diagrams. The fits have been carried out over a limited frequencies range spreading from 100 to 0.01 Hz. This approach allows avoiding the interaction between the electrical wires inductance with the first semicircle of the spectrum. This circuit is composed by the combination of:

- a pure resistance R_{HF} at the highest frequencies,
- a resistance R_{MF} in parallel with a Constant Phase Element CPE_{MF} at the intermediate frequencies,
- a resistance R_{LF} in parallel with a Constant Phase Element CPE_{LF} at the lowest frequencies.

It has been found that the 'redox' cycles have an impact on the spectra which is illustrated in Fig. 10. On one hand the value of R_{HF} has been strongly increased. On the other hand, the size of the semicircle ranging at the middle frequencies has risen. These evolutions have been quantified through the fits performed on data obtained at each cycle. Fig. 11 gives the evolution of R_{HF} and R_{MF} cell resistances as a function of the cycle number. It can be noticed that the semicircle at the lowest frequencies is remained nearly stable during the test (in fact, it has increased from 0.40 Ω cm^2 after the first 'redox' cycle to 0.44 Ω cm^2 after the eighth 'redox' cycle).

It is worth to underline that the increase in size of the MF semicircle has occurred without a change of its relaxation frequency (Fig. 10). Indeed, this characteristic frequency is remained equal to 89 ± 4 Hz during the test (for a confidence interval of 68%). This result means that the electrochemical mechanisms characterised by the relaxation frequencies have not been impacted by the 'redox' cycles. Thus, a mechanical damage along the electrochemical interfaces can be proposed to explain the electrochemical degradation. Indeed, the cracking must induce a local modification of the

Table 2
Material properties used for the mechanical calculations.

	Elastic parameters		
	Young Modulus E (GPa)	Poisson ratio ν	Thermal expansion coefficient α (=10^{-6} K^{-1})
NiO-8YSZ substrate (ACC) (porosity = 23%)	112.3 [20,21]	0.284 [20,21]	12.5*
NiO-8YSZ functional layer (AFL) (porosity = 5%)	184.8 [20,21]	0.311 [20,21]	12.5*
Ni-8YSZ substrate (ACC) (porosity = 43%)	56.8 [20,21]	0.258 [20,21]	12.5[22]
8YSZ	190 [23]	0.308 [23]	10.8 [24,25]
LSM	35.0 [26]	0.36 [27]	11.7 [25]

	Fracture parameters				
	Fracture toughness G_c (J m^{-2})	Weibull modulus m	Characteristic strength σ_0 (MPa)	Reference volume (mm^3)	Interfacial toughness G_c (J m^{-2})
8YSZ**	6.7 [28]	8 [28]	282 [28]	0.27 [28]	–
NiO-8YSZ//8YSZ	–	–	–	–	~10 [11]

* Assumed to be equal to Ni-YSZ.
** Values given for 900 °C.

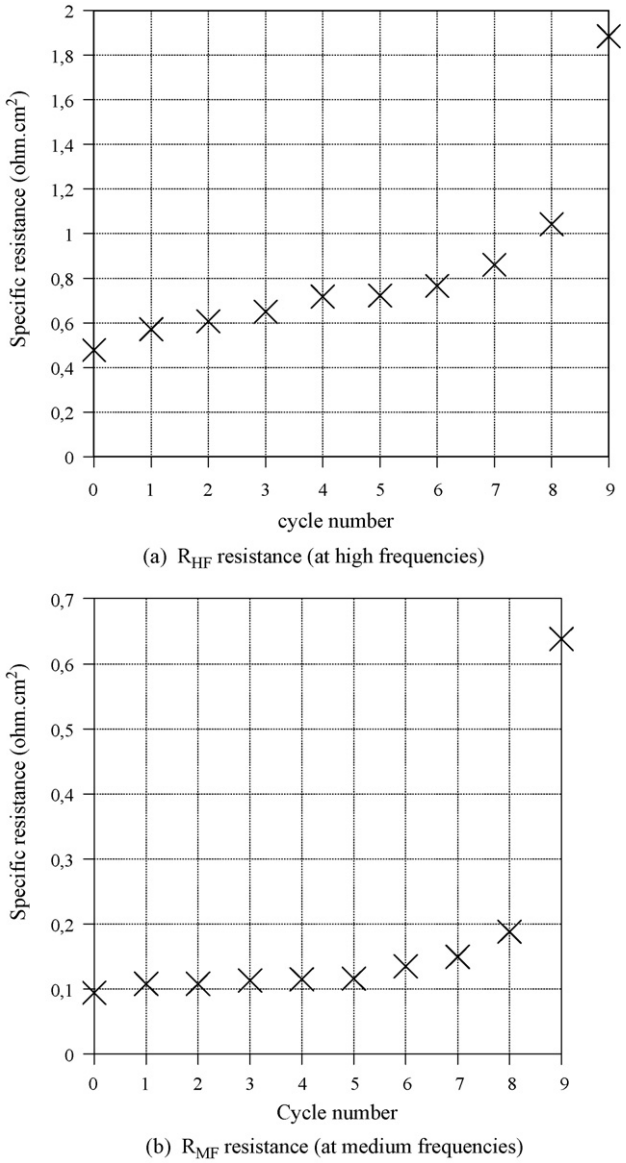

Fig. 11. (a) R_{HF} resistance (at high frequencies). (b) R_{MF} resistance (at medium frequencies). R_{HF} and R_{MF} resistances plotted as function of the cycle number.

electrodes geometry. This lost in active area leads to an increase in the ohmic and polarisation cell resistances, without modifications on the cell frequency response.

4. Discussion

4.1. Cell damage after anode re-oxidation induced by an air stream

It has been shown that the electrolyte rupture is triggered at 800 °C for a critical oxidation degree ranging between ~58 and ~71%. This fracture threshold is found to be in good agreement with the one established by Sarantaridis et al. [13] on cells with the same anode cermet microstructure. Indeed, these authors have detected the electrolyte rupture for a conversion of Ni into NiO of 49–75%. In other words, the oxidation strain ε_{ox} should not exceed a value ranging between 0.26 and 0.34% for this cermet microstructure at 800 °C. It is worth to underline that this threshold has been obtained on free standing cells. This result is transferable to stack configuration only if the glass seal maintaining the cell in the interconnect housing is viscous at 800 °C. In this condition, the cell will be not constrained at its periphery upon oxidation.

The level of the cermet oxidation related to the electrolyte failure, which has been assessed experimentally, can be compared with the value found by an energetic or a statistic modelling of fracture.

Because of the manufacturing process or the anode oxidation, the cermet substrate undergoes some volume changes. These contractions or expansions generate an equi-biaxial stress $\sigma_{\text{equi-biaxial}}$ in the electrolyte film (*i.e.*, the radial stress σ_{rr} is equal to the circumferential stress $\sigma_{\theta\theta}$). This stress field is the sum of one contribution due to the manufacturing process $\sigma_{\text{manufacturing}}$ [10,17] and one contribution due to the anode oxidation $\sigma_{\text{oxidation}}$ [10]. The impact of the cathode layer on the cell stress state being negligible [10], the equi-biaxial stress of the thin electrolyte can be expressed by the following equations:

$$\sigma_{\text{equi-biaxial}} = \sigma_{\text{manufacturing}} + \sigma_{\text{oxidation}} \quad \text{with } \sigma_{\text{manufacturing}} = \frac{(\alpha_{\text{NiO-YSZ}} - \alpha_{\text{YSZ}})(T_{\text{oxidation}} - T_{\text{manufacturing}})}{(1-\nu_{\text{YSZ}})/E_{\text{YSZ}} + (h_{\text{electrolyte}}/h_{\text{anode}})(1-\nu_{\text{NiO-YSZ}})/E_{\text{NiO-YSZ}}}$$

$$\text{and } \sigma_{\text{oxidation}} = \frac{E_{\text{YSZ}}}{(1-\nu_{\text{YSZ}})}\varepsilon_{ox} \tag{4}$$

where α, E and ν are respectively the Thermal Expansion Coefficient (TEC), the Young's modulus and the Poisson's ratio of the electrolyte layer or NiO-YSZ cermet substrate. The term $T_{\text{oxidation}}$ denotes the temperature during the oxidation treatment (=800 °C) whereas

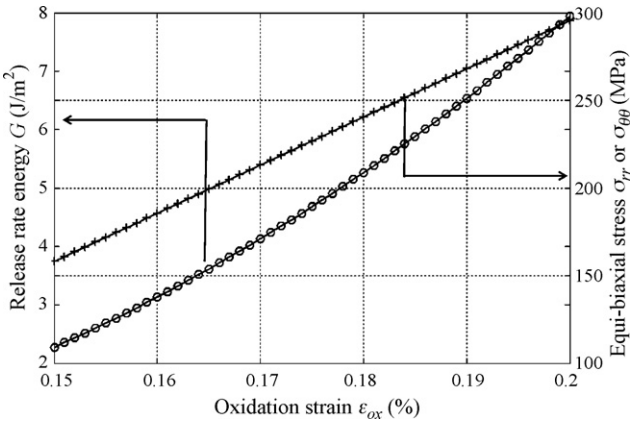

Fig. 12. Equi-biaxial stress and release rate energy related to the channel cracking mechanisms (electrolyte) plotted as a function the cermet oxidation strain. The material properties used for the calculation are given in Table 2.

$T_{manufacturing}$ represents the anode/electrolyte co-sintering temperature (=1350 °C). The term ε_{ox} corresponds to the irreversible linear strain of the cermet due to its re-oxidation.

(a) *Energetic approach:* the following equation describes the energy release rate G corresponding to the energy available for the channel cracking through the electrolyte [18]:

$$G = Z \times \frac{1-\nu_{YSZ}}{E_{YSZ}} \times \sigma^2_{equi\text{-}biaxial} \times h_{electrolyte} \quad (5)$$

Assuming neither substrate penetration nor channel interaction, the dimensionless parameter Z depends only on the mismatch in elastic parameters between the substrate and the film. This elastic mismatch is characterised by the Dundurs parameters α, β. For the NiO-8YSZ//8YSZ bi-material, the values are $\alpha = 0.264$, $\beta = 0.088$ leading to a value of Z roughly equal to 2.5 [18]. It can be noticed that the observed crack spacing (~155 μm) is higher than $8 \times h_{electrolyte}$, meaning that the assumption of no crack interaction is justified [19].

Fig. 12 illustrates the rising in the energy release rate G with the oxidation strain ε_{ox} calculated according to Eqs. (4) and (5). Cracking is assumed to occur when G reaches the electrolyte fracture toughness $G_c = 6.7\ J\ m^{-2}$ (cf. Table 2). With this model, the critical oxidation strain is found to be equal to ~0.19%.

(b) *Statistical approach:* according to the Weibull's theory, the survival probability P_s of the electrolyte layer is given by Eq. (6) [10]. The term P_s is expressed as the product of the survival probability determined for the two principal stresses, $\sigma_{\theta\theta}$ and σ_{rr} (=$\sigma_{equi\text{-}biaxial}$):

$$P_s = \exp\left(-\frac{V_{electrolyte}}{V_0}\left(\frac{\sigma_{rr}}{\sigma_0}\right)^m\right) \times \exp\left(-\frac{V_{electrolyte}}{V_0}\left(\frac{\sigma_{\theta\theta}}{\sigma_0}\right)^m\right)$$
$$P_s = \left\{\exp\left(-\frac{V_{electrolyte}}{V_0}\left(\frac{\sigma_{equi\text{-}biaxial}}{\sigma_0}\right)^m\right)\right\}^2 \quad (6)$$

where V_0, σ_0 and m are the Weibull parameters related to the 8YSZ material (see Table 2). The term $V_{electrolyte}$ denotes the electrolyte volume. The dependence of P_s with the oxidation strain ε_{ox} is plotted in Fig. 13. The survival probability is found to fall down to 0 for a critical oxidation strain of ~0.16%: this value can be considered as the threshold for which the electrolyte failure is triggered.

A rather good agreement is obtained between the critical oxidation strains determined by the energetic and probabilistic approaches. However, in both cases the critical oxidation strains are found to be below the experimental value (between 0.26 and 0.34%). This slight discrepancy between the predicted and measured thresholds could be attributed to the inappropriate material data used for the calculations. Indeed, values of toughness and the Weibull parameters reported in Table 2 have been determined on a thick tape-cast 8YSZ substrate (~100 μm) tested at 900 °C [28] whereas the present experiments have been carried out at 800 °C considering a thin vacuum slip casting 8YSZ deposit (10 μm). These experimental data have been used because of a lack of more reliable values. However it is expected that the mechanical properties depend on the layer characteristics. Therefore, the mechanical parameters used in the present analysis could lead to underestimate the real strength at 800 °C of the thin electrolyte film.

The actual toughness and the Weibull parameters of the thin electrolyte layer may be indirectly estimated from the spacing of the electrolyte cracks [29,30]. It is out of the scope of this paper to deal with this technique which is going to be investigated by the authors.

However, the calculated critical oxidation strain (0.16–0.19%) is safe regarding to the cell integrity. It corresponds to a critical oxidation degree of 50% which can be considered as a conservative limit to preserve the cell.

4.2. Cell damage after anode re-oxidation induced by an ionic current

4.2.1. Analysis of impedance diagrams evolution during the test

Cell degradation has been characterised by impedance spectroscopy after each anode re-oxidation step. A seen in Figs. 10 and 11, high frequency resistance and size of the first semicircle at intermediate frequencies have been found to increase drastically during the test. Since no shift in the diagram frequencies has been observed, it has been concluded that the modification of the cell response is only due to a mechanical damage localised on the electrochemical interfaces.

The first semicircle of the impedance diagrams presents a frequency relaxation close to 100 Hz. On the basis of previous studies [31–34], this first semicircle can be attributed to the Ni-YSZ cermet response. This remark means that the degradation is only restricted to the anode side. Therefore, the observed cell degradation can be attributed to a mechanical damage arising in a region close to the anode/electrolyte interface.

The impedance diagrams evolution (Figs. 10 and 11) can be interpreted according to the results established by Gazzori and Kesler [35–37]. Indeed, these authors have shown by a modelling approach that a delamination induces an increase in both the high frequency

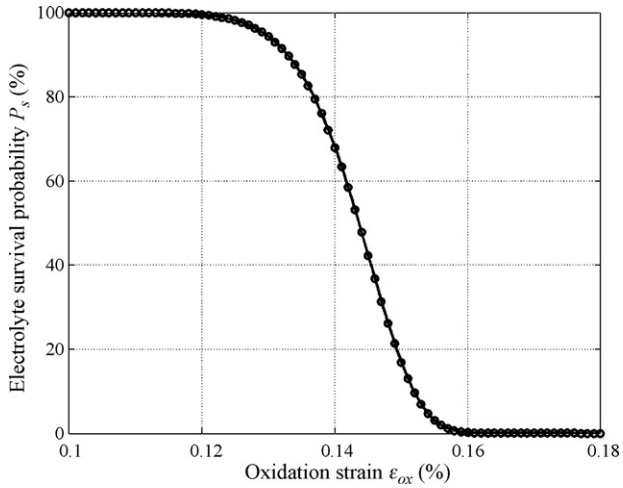

Fig. 13. Electrolyte survival probability calculated as a function of the oxidation strain. The material properties used for the calculation are given in Table 2.

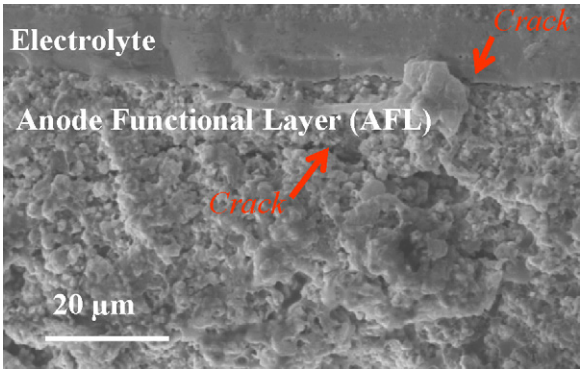

Fig. 14. SEM observation of the cell cross-section (after the 'redox' cycles). Interfacial cracks have been initiated on each side of the AFL.

intercept and semicircle size of the impedance diagrams. Furthermore, they found that the peak of frequency of the electrodes semicircle remains unchanged as there is no change in the electrochemistry of the system upon delamination. Therefore, it can be concluded that evolution of impedance diagrams measured in the present study (Figs. 10 and 11) can be attributed to a delamination at the ACC/AFL or AFL/electrolyte interfaces.

The interpretation of impedance diagrams evolution is found to be consistent with the cell damage observed by post-test analysis. A representative cell cross-section examined in a SEM after test is reported in Fig. 14. Cracks are observed both along the ACC/AFL and AFL/electrolyte interfaces.

4.2.2. Mechanical analysis of the cell damage

Waldbillig et al. [6] and Hatae et al. [14] mentioned that, if the electrochemical oxidised layer is thin regarding the anode thickness, it will be constrained by the substrate in its reduced state on one side and by the dense electrolyte on the other side. In this condition, the cermet layer cannot expand upon oxidation, and compressive stresses will be generated in the oxidised cermet and may induce delamination.

The reliability of this assumption has been verified in the case of the present study. For this purpose, the thickness of the re-oxidised layer has been assessed and a mechanical analysis had been performed.

(a) *Thickness of the oxidised layer:* According to Eq. (1), the Ni electrochemical oxidation rate is governed by the imposed current density (*i.e.*, the O^{2-} flux through the electrolyte). The extension of the re-oxidised layer from the anode/electrolyte interface, h, can be estimated trough a simple oxygen molar balance: the following equation has been established assuming that each particle of Nickel is completely oxidised:

$$h = \frac{\Delta m}{C_{Ni} \times (1-\varepsilon) S_{cell} d_{Ni}} \quad \text{with } \Delta m = \frac{I}{2F} \Delta t \, M_{Ni} \tag{7}$$

where S_{cell} corresponds to the cell active area, F is the Faraday's constant (=96,500 C mol^{-1}) and I represents the current. The terms M_{Ni} and d_{Ni} denote respectively the molar mass and the density of Nickel. The parameter ε is the cermet porosity which is around 20% for the anode functional layer and 40% for current collector substrate. C_{Ni} is the Nickel content of the cermet (40 vol.%).

In order to check the validity of this model, the data of Hatae et al. [14] have been considered. These authors have electrochemically oxidised a classical Ni-YSZ cermet. Under a current of 7.5 mA cm^{-2} applied for 30 min, they have observed by SEM that only the Anode Functional Layer (~20 µm) is fully re-oxidised. It is worth to underline that the numerical application of Eq. (7) gives a thickness for the NiO-YSZ layer equal to 19 µm. The good agreement between these experimental and calculated values proves the reliability of Eq. (7).

In the case of the present study, this approach has been used to assess the ratio of NiO layer thickness over the total anode thickness. The results reported in Table 2 show that, whatever the cycle, only a small part of the cermet has been re-oxidised.

(b) *Mechanical analysis:* To establish the occurrence of the delamination, the numerical tool presented in reference [10] has been used to calculate the stress field after the anode re-oxidation. The cathode, electrolyte, AFL and ACC layers have been described into the present analysis. It is reminded that the simulations, based on a Finite Element Method (FEM), are carried out by considering a pure elastic behaviour of the cell materials.

The stress field is calculated as the sum of one contribution, $\sigma_{manufacturing}$, due to the manufacturing process and a second contribution, $\sigma_{oxidation}$, due the anode oxidation. To estimate this last term, it has been assumed that the ACC remains in its reduced Ni-YSZ state during the 'redox' cycle. In other words, it has been assumed that only AFL is oxidised, and then, undergoes an irreversible strain ε_{ox}. Indeed, since the porosity of the functional layer is two times lower than the porosity the current collecting substrate, the oxidation strain of the functional layer is expected to be much higher than the one of the remaining anode [6].

The equi-biaxial stress for the cathode, electrolyte and AFL is plotted in Fig. 15. It has been expressed as a function of the AFL oxidation strain. It is found that the compressive stress in the electrolyte is slightly decreased after the AFL re-oxidation. This result is in good agreement with the RX measurements carried out by Hatae et al. [14]. Indeed, these authors have shown that the residual stress in the electrolyte is partially relaxed by the expansion of the Ni particles after passing the ionic current.

Even for low values of the applied oxidation strain, ε_{ox}, a high compressive stress is highlighted in the AFL (Fig. 15). For instance, the stress level reaches −470 MPa for an AFL oxidation strain of only 0.2%. This result is explained because the ACC substrate prevents the bulk expansion of the thin oxidised layer. Under this specific stress state, a shear stress component, τ, is generated in the oxidised layer. Therefore, the porous AFL failure could be initiated under mode II cracking in the direction for which the shear stress is the maximum ($\sigma_{equi\text{-}biaxial} = \tau_{max}$ at 45° from the ACC/AFL plane).

This failure initiation could lead to crack propagation in the ACC/AFL interface. Indeed, the energy available for the delamina-

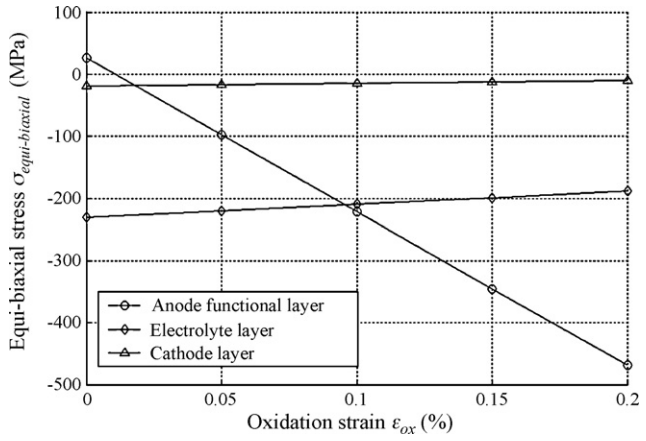

Fig. 15. The equi-biaxial stress is plotted as a function of the oxidation strain of the anode functional layer. The material properties used for the simulations are given in Table 2.

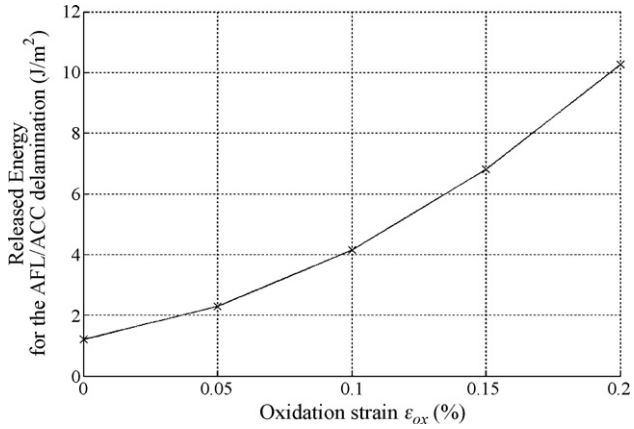

Fig. 16. Released energy for the complete debonding of the ACC/AFL interface. The material properties used for the simulations are given in Table 2.

tion of this interface has been estimated according to Eq. (8) and plotted in Fig. 16 as a function of the AFL bulk expansion:

$$G = \sum_{i=1}^{i=4} \left(\frac{1-\nu_i}{E_i} \times \sigma^2_{\text{equi-biaxial},\,i} \times h_i \right) - \sum_{i=1}^{i=3} \left(\frac{1-\nu_i}{E_i} \times \sigma^2_{\text{equi-biaxial},\,i} \times h_i \right) \quad (8)$$

where the subscript i denotes the cathode for $i=1$, the electrolyte for $i=2$, the AFL for $i=3$ and the ACC for $i=4$. This released energy increases with the AFL bulk expansion increase. It is found that G exceeds $10\,\text{J m}^{-2}$ for an oxidation strain of 0.2%.

It has been demonstrated that the ACC/AFL interface is weaker than the electrolyte/AFL interface [38]. As the fracture energy of the electrolyte/AFL interface is estimated to be around $10\,\text{J m}^{-2}$ (see Table 2), it can be concluded that the interfacial toughness of the ACC/AFL interface is lower than $10\,\text{J m}^{-2}$. Under this condition, the present mechanical analysis suggests that the ACC/AFL delamination is likely to occur, even for a loading corresponding to a partial re-oxidation of the functional layer. This failure mechanism is found to be consistent with the experimental results.

5. Conclusion

In the case of fuel starvation or fuel shutdown, a methodology has been proposed to evaluate the ASC degradations due to the cermet re-oxidation. This methodology has been applied to state the mechanical damage of typical SOFC cells (provided by FZJ research centre).

For Cermet re-oxidation caused by an air stream, the oxidation degree threshold from which the electrolyte fracture is triggered has been determined: the electrolyte cracking has been found to occur for a degree of oxidation ranging between ~58 and ~71%. Mechanical analyses based on energetic and probabilistic approaches of fracture have been performed. Both analysis exhibit relatively close results and predict an electrolyte failure for a critical degree of oxidation equal to around 50%. The calculated threshold is sensibly lower than the experimental one. This discrepancy between the experiments and the calculations has been attributed to the use of non-appropriate material data (relative to a thick 8YSZ substrate and not a thin 8YSZ layer).

The effect of cermet re-oxidation induced by an ionic current has been also investigated. Impedance spectroscopy has been used to estimate the electrochemical degradations. The evolution of the impedance diagrams after each 'redox' cycle has been explained by a cermet damage arising in a region close to anode/electrolyte interface. This conclusion is found to be in good agreement with the result obtained with a mechanical analysis of the test. This analysis has shown that the AFL re-oxidation leads to a high compressive stress in this layer. Under this specific loading, a delamination at the AFL/ACC interface is expected.

Acknowledgments

The authors would like to thank Mr. B. Sommacal and Mr. H. Giraud for their technical contributions and Dr. S. Rosini for many useful discussions. Part of this work has been obtained in the framework of national research programs led by Mr. S. Hody from GdF/Suez and supported by the French Research Agency (Pan-H). The authors would like to thank Dr. N.H. Menzler and Dr. R. Steinberger-Wilckens from Forschungszentrum Jülich for the critical reading of the paper and for providing the cells in the frame of the Real-SOFC project (project supported by the European Union: contract number SES6-CT-2003-502612).

References

[1] D. Waldbillig, A. Wood, D.G. Ivey, J. Power Sources 145 (2005) 206–215.
[2] J. Kong, K. Sun, D. Zhou, N. Zhang, J. Qiao, Rare Metals 25 (2006) 300–304.
[3] B. Liu, Y. Zhang, B. Tu, Y. Don, M. Cheng, J. Power Sources 165 (2007) 114–119.
[4] M.C. Tucker, G.Y. Lau, C.P. Jacobson, L.C. De Jonghe, S.J. Visco, J. Power Sources 175 (2008) 447–451.
[5] T. Klemenso, C. Chung, P.H. Larsen, M. Mogensen, J. Electrochem. Soc. 152 (11) (2005) A2186–A2192.
[6] D. Waldbillig, A. Wood, D.G. Ivey, Solids State Ion. 176 (2005) 847–859.
[7] M. Cassidy, G. Lindsay, K. Kendall, J. Power Sources 61 (1996) 189–192.
[8] M. Ettler, G. Blaß, N.H. Menzler, Fuel Cells 7 (5) (2007) 349–355.
[9] J. Malzbender, E. Wessel, R.W. Steinbrech, Solid State Ion. 176 (2005) 2201–2203.
[10] J. Laurencin, G. Delette, F. Lefebvre-Joud, M. Dupeux, J. Eur. Ceram. Soc. 28 (2008) 1857–1869.
[11] D. Sarantaridis, A. Atkinson, The 7th European Fuel Cell Forum (Switzerland), 2006, paper P0728.
[12] D. Sarantaridis, A. Atkinson, Fuel Cells 3 (2007) 246–258.
[13] D. Sarantaridis, R.A. Rudkin, A. Atkinson, J. Power sources 180 (2008) 704–710.
[14] T. Hatae, Y. Matsuzaki, Y. Yamazaki, Solid State Ion. 179 (2008) 274–281.
[15] W.A. Meulenberg, N.H. Menzler, H.P. Buchkremer, D. Stöver, in: A. Manthiram, P.N. Kumta, S.K. Sundaram, G. Ceder (Eds.), Ceramic Transactions: Materials for Electrochemical Energy Conversion and Storage, vol. 127, American Ceramic Society, Westerville, OH, 2002, pp. 99–108.
[16] D. Larrain, J. Van Herle, D. Favrat, J. Power Sources 161 (2006) 392–403.
[17] W. Fisher, J. Malzbender, G. Blass, R.W. Steinbrech, J. Power Sources 150 (2005) 73–77.
[18] J.W. Hutchinson, Z. Suo, Adv. Appl. Mech. 29 (1992) 63–191.
[19] F. Delannay, P. Warren, Acta Metall. Mater. 39 (6) (1991) 1061–1072.
[20] M. Radovic, E. Lara-Curzio, Acta Mater. 52 (2004) 5747–5756.
[21] M. Radovic, E. Lara-Curzio, J. Am. Ceram. Soc. 87 (12) (2004) 2242–2246.
[22] F. Tietz, Ionics 5 (1999) 129–139.
[23] A. Atkinson, A. Selçuk, Solids State Ion. 134 (2000) 59–66.
[24] S.T. Aruna, M. Muthuraman, K.C. Patil, Solids State Ion. 111 (1998) 45–51.
[25] A. Nakajo, C. Stiller, G. Härkegard, O. Bolland, J. Power Sources 158 (2006) 287–294.
[26] T. Nishikawa, D. Ogawa, S. Honda, H. Awaji, J. Soc. Mater. Sci. (Jpn.) 52 (6) (2003) 587–591.
[27] G. Fehringer, S. Janes, M. Wildersohn, R. Clasen, J. Eur. Ceram. Soc. 24 (2004) 705–715.
[28] A. Selçuk, A. Atkinson, J. Am. Ceram. Soc. 83 (8) (2000) 2029–2035.
[29] P. Scafidi, M. Ignat, M. Dupeux, Mat. Res. Soc. Symp. Proc. 300 (1993) 55–60.
[30] A. Mézin, Acta Metall. Mater. 43 (8) (1995) 3151–3157.
[31] M. Guillodo, P. Vernoux, J. Fouletier, Solid State Ion. 127 (2000) 99–107.
[32] T.L. Reitz, H. Xiao, J. Power Sources 161 (2006) 437–443.
[33] H. Xiao, T.L. Reitz, M.A. Rottmayer, J. Power Sources 183 (2008) 49–54.
[34] M. Lang, C. Auer, A. Eismann, P. Szabo, N. Wagner, Electrochim. Acta 53 (2008) 7509–7513.
[35] J.I. Gazzari, O. Kesler, J. Power Sources 167 (2007) 100–110.
[36] J.I. Gazzari, O. Kesler, J. Power Sources 167 (2007) 430–441.
[37] J.I. Gazzari, O. Kesler, J. Power Sources 176 (2008) 138–154.
[38] Y. Xie, X. Zhang, M. Robertson, R. Maric, D. Ghosh, J. Power Sources 162 (2006) 436–443.